



The Nature of Luminous Quasars with Very Large C IV Equivalent Widths

SHUQI FU ^{1,2} W. N. BRANDT ^{3,4,5} FAN ZOU ^{3,4} ARI LAOR ⁶ GORDON P. GARMIRE ⁷ QINGLING NI ⁸
JOHN D. TIMLIN III ^{3,4} AND YONGQUAN XUE ^{1,2}

¹CAS Key Laboratory for Research in Galaxies and Cosmology, Department of Astronomy, University of Science and Technology of China, Hefei 230026, China

²School of Astronomy and Space Sciences, University of Science and Technology of China, Hefei 230026, China

³Department of Astronomy and Astrophysics, 525 Davey Lab, The Pennsylvania State University, University Park, PA 16802, USA

⁴Institute for Gravitation and the Cosmos, The Pennsylvania State University, University Park, PA 16802, USA

⁵Department of Physics, 104 Davey Laboratory, The Pennsylvania State University, University Park, PA 16802, USA

⁶Physics Department, Technion, Haifa 32000, Israel

⁷Huntingdon Institute for X-ray Astronomy, LLC, 10677 Franks Road, Huntingdon, PA 16652, USA

⁸Institute for Astronomy, University of Edinburgh, Royal Observatory, Edinburgh EH9 3HJ, UK

ABSTRACT

We report results for a complete sample of ten luminous radio-quiet quasars with large C IV equivalent widths ($EW \geq 150 \text{ \AA}$). For 8/10 we performed Chandra snapshot observations. We find that, in addition to the enhanced C IV line EW, their He II and Mg II lines are enhanced, but the C III] line is not. Their X-ray emission is substantially stronger than expected from their ultraviolet luminosity. Additionally, these large C IV EW quasars show small C IV blueshifts and possibly low Eddington ratios, suggesting they are “extreme low Eigenvector 1 (EV1)” quasars. The mean excess He II EW is well-matched by Radiation Pressure Compression (RPC) photoionization models, with the harder α_{ox} ionizing spectrum. However, these results do not reproduce well the enhancement pattern of the C IV, Mg II, and C III] EWs, or the observed high C IV/Mg II ratio. RPC calculations indicate that the C IV/Mg II line ratio is an effective metallicity indicator, and models with sub-Solar metallicity gas and a hard ionizing continuum reproduce well the enhancement pattern of all four ultraviolet lines. We find that the C IV/Mg II line ratio in quasars is generally correlated with the excess X-ray emission. Extremely high EV1 quasars are characterized by high metallicity and suppressed X-ray emission. The underlying mechanism relating gas metallicity and X-ray emission is not clear, but may be related to radiation-pressure driven disk winds, which are enhanced at high metallicity, and consequent mass loading reducing coronal X-ray emission.

Keywords: Quasars (1319), X-ray quasars (1821), Photoionization (2060), Metallicity (1031)

1. INTRODUCTION

Quasars are distinguishable from other astronomical sources by the typical presence of broad emission lines in their optical/ultraviolet (UV) spectra. These broad lines contain a wealth of information about the underlying physical properties of quasars. In particular, the C IV broad emission line in luminous quasars has been the target of extensive research. C IV $\lambda 1549$ rest-frame equivalent width (C IV EW) and blueshift are known to correlate with the UV–X-ray power-law slope (α_{ox} ;¹ e.g., Green 1998; Gibson et al. 2008; Richards et al. 2011;

Timlin et al. 2020) and to be linked to the Eddington ratio (i.e., the ratio between the bolometric luminosity and the Eddington luminosity; e.g., Baskin & Laor 2004; Shen & Ho 2014; Rivera et al. 2020). Additionally, X-ray studies of Sloan Digital Sky Survey (SDSS; York et al. 2000) quasars have confirmed a positive correlation between C IV EW and $\Delta\alpha_{\text{ox}}$,² a parameter quantifying the strength of the X-ray emission compared to that of a typical quasar matched in UV luminosity (Gibson et al. 2008; Timlin et al. 2020). Physically, this correlation is likely expected since there are more X-ray/EUV

¹ $\alpha_{\text{ox}} = 0.3838 \times \log_{10}(f_{2\text{keV}}/f_{2500})$, where $f_{2\text{keV}}$ and f_{2500} are the flux density at rest-frame 2 keV and 2500 Å, respectively.

² $\Delta\alpha_{\text{ox}} = \alpha_{\text{ox}} - \alpha_{\text{ox}}(L_{2500})$, where $\alpha_{\text{ox}}(L_{2500})$ is the expected α_{ox} at a specified value of L_{2500} from the relation in Just et al. (2007).

(extreme UV) ionizing photons to produce C IV ions in quasars with stronger X-ray emission. The quasars in these correlation studies have C IV EWs largely in the range 20–100 Å due to the rarity of quasars outside this C IV EW range. Survey observations, however, have found a small population of luminous radio-quiet quasars that have very large C IV EWs (C IV EW $\gtrsim 150$ Å) as well as radio-quiet quasars with extraordinarily weak lines (C IV EW $\lesssim 15$ Å). X-ray observations of weak-line quasars (WLQs) continue to provide insights into the nature of these objects; however, the X-ray and other properties of luminous quasars with very large C IV EWs have not been well studied.

WLQs are a prime example of how these rare populations exhibit extraordinary X-ray properties. For example, nearly half of WLQs have been observed to be X-ray weak ($\Delta\alpha_{\text{ox}} \leq -0.2$; e.g., Luo et al. 2015; Ni et al. 2018, 2022), many of which are weak by factors of ≈ 20 –80 or more with respect to typical quasars (e.g., Just et al. 2007), and appear to be significantly X-ray absorbed. The other half have nominal-strength X-ray emission ($\Delta\alpha_{\text{ox}} \approx 0$). WLQs appear to have large Eddington ratios as indicated by their steeper intrinsic X-ray power-law continua with respect to typical quasars (Luo et al. 2015; Marlar et al. 2018). The high incidence of X-ray weakness among WLQs is not observed in the general quasar population. As part of their work, Ni et al. (2018, 2022) generated a representative, unbiased sample of 32 WLQs (and 63 total WLQs) to investigate further the $\Delta\alpha_{\text{ox}} - \text{C IV EW}$ relation and found that the WLQs exhibit a strikingly large dispersion around the best-fit trend derived for typical quasars. X-ray observations of the rare population of quasars with very large C IV EWs might find similarly notable properties and furthermore help to constrain better the $\Delta\alpha_{\text{ox}} - \text{C IV EW}$ correlation.

To increase the dynamic range of C IV EW coverage and improve the significance of the $\Delta\alpha_{\text{ox}} - \text{C IV EW}$ correlation, Timlin et al. (2020) (hereafter T20) searched for serendipitous Chandra observations of quasars in the SDSS fourteenth data release (DR14Q, Pâris et al. 2018). Quality cuts were imposed on the data (e.g., cuts in redshift and on sensitivity of the Chandra observations) to generate an unbiased sample of quasars with a high X-ray detection fraction. The final “Sensitive” sample contains 753 typical quasars with X-ray flux measurements, 637 of which also have C IV EW measurements (hereafter the “C IV subsample”). T20 found that the strength of the ionizing emission remains positively correlated with C IV EW even after accounting for the dependence of α_{ox} on L_{2500} (represented by $\Delta\alpha_{\text{ox}}$). However, the T20 serendipitous sample in-

cluded few quasars with very large C IV EWs (≥ 150 Å), making it unclear if the correlation fitted to the typical quasars can be appropriately extrapolated to larger C IV EWs.

Many of the quasars with very large C IV EWs (150 – 185 Å) included in the T20 sample are much less luminous than the full sample and currently studied WLQs. Large C IV EWs are rarely found for luminous quasars due to the observed anti-correlation between quasar continuum luminosity and C IV EW (the Baldwin effect; Baldwin 1977). Among the 637 quasars in the T20 sample, only two have large C IV EWs (C IV EW $\gtrsim 150$ Å) and relatively large rest-frame 2500 Å luminosity ($L_{2500} \gtrsim 10^{30.5}$ erg s $^{-1}$ Hz $^{-1}$). These two quasars differ in X-ray strength (measured by α_{ox}) by a factor of ≈ 3.5 , making it difficult to determine if this outlier population has X-ray properties consistent with the general quasar population or if it has notable properties analogously to WLQs. We therefore proposed Chandra snapshot observations of eight quasars with large C IV EWs to understand better the relation between their X-ray continuum and UV emission-line strengths.

Studies of such extreme objects can also help to clarify the dependence of quasar broad line emission upon factors including ionizing continuum strength and metallicity. For example, photoionization calculations have shown that while the strengths of two well-studied high-ionization emission lines, C IV and He II $\lambda 1640$, both depend upon the strength of the EUV ionizing radiation, they have different sensitivities to the metallicity of the quasar broad emission-line region gas (e.g., see Figure 5 of Baskin et al. 2014). Higher metallicity cools the gas, and weakens the C IV line. The He II line, on the other hand, provides a relatively “clean” measure of the number of ionizing photons, and is nearly independent of metallicity. The targeted quasars with large C IV EW should allow us to test this and related behavior over a wide range of parameters.

This paper is organized as follows. In Section 2 we describe the sample selection, our Chandra observations and data reduction, and the optical spectral-fitting methods. In Section 3 we show our main findings regarding the distinct optical and X-ray properties of our target quasars. Possible explanations of their observed properties are given in Section 4. Finally, Section 5 summarizes the results. Throughout this work, we adopt a flat Λ -CDM cosmology with $H_0 = 70$ km s $^{-1}$ Mpc $^{-1}$, $\Omega_M = 0.3$, and $\Omega_\Lambda = 0.7$.

2. SAMPLE SELECTION AND DATA

2.1. Sample selection

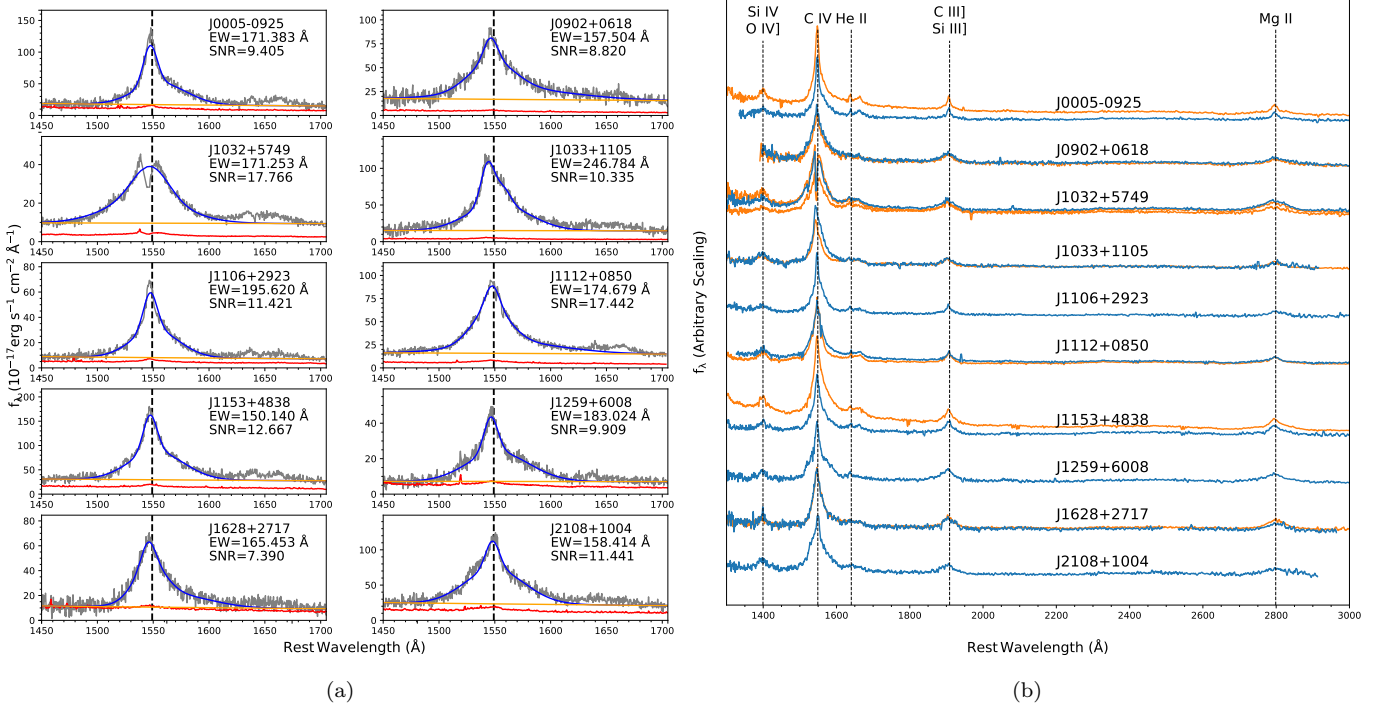


Figure 1. (a) The C IV line region of the SDSS DR7 spectra of the eight target quasars and two large C IV EW quasars from T20 (SDSS J103215.88+574926.4 and SDSS J125929.13+600846.0) included in our sample. The grey, red, blue, and orange lines are data, error, three broad Gaussian profiles, and local power-law continuum, respectively. The vertical dashed lines show the laboratory wavelengths of the C IV line ($\lambda = 1549.06 \text{ \AA}$). The rest-frame equivalent width (\AA) of the C IV line measured from the Gaussian models and the median signal-to-noise ratio (SNR) per pixel for the C IV line are listed in the upper right. These C IV lines have high spectral quality (SNR > 7) and large rest-frame equivalent widths (EW $> 150 \text{ \AA}$). (b) All the available UV emission lines. The SDSS DR7 spectra are shown in blue, while other observations, if any, are shown in orange.

We selected our targets from the Shen et al. (2011) quasar catalog, which contains 17 quasars that have C IV EW $\geq 150 \text{ \AA}$. We also require our targets to be optically bright (i -band magnitude < 20) and not significantly red compared to typical quasars or WLQs ($\Delta(g - i) \leq 0.15^3$; see Richards et al. 2003), and to have no previous sensitive X-ray coverage. A total of eight quasars were selected with redshifts ranging from 1.7–2.2. We adopted the improved redshift measurements from Hewett & Wild (2010), based on cross-correlation (with a master quasar template) that includes Mg II $\lambda 2799$ or C III] $\lambda 1908$, as the systemic redshifts for the target quasars, which have systematic biases a factor of ≈ 20 lower compared to the SDSS pipeline redshift values. We also inspected their SDSS spectra visually, and no broad absorption lines are present. Our targets are also more luminous (with a median $M_i = -26.4$; see Table 1) than the quasars in

the T20 sample that have comparable C IV EWs except for the two with similar UV luminosities mentioned in Section 1. These two, SDSS J103215.88+574926.4 and SDSS J125929.13+600846.0, will be included in the following analyses due to their similarity to our new sources (see Section 3). The C IV line regions of the SDSS DR7 spectra of the ten quasars are shown in Figure 1a, and the whole spectra are shown in Figure 1b.

These ten quasars are observed to be radio quiet in the Very Large Array FIRST survey (Becker et al. 1995). We derived 2σ upper limits on the 20 cm radio flux as $0.25 + 2\sigma_{\text{rms}}$ mJy, where σ_{rms} is the RMS flux at the source position and 0.25 mJy is the CLEAN bias correction (White et al. 1997), and we obtain flux densities at rest-frame 2500 \AA (f_{2500}) by converting $M_i(z = 2)$ (Richards et al. 2006) to monochromatic luminosity at 2500 \AA (L_{2500}) and then converting L_{2500} to f_{2500} .⁴ Then we calculate the upper limits on the radio-loudness

³ Relative color, defined by subtracting the median colors of quasars at the redshift of each quasar from the measured colors of each quasar.

⁴ $L_{2500} = 4\pi D_L^2 f_{2500} / (1+z)$, where D_L is the luminosity distance.

parameter R ,⁵ and all of our targets have $R < 5$. Thus no additional strong X-ray emission is expected due to quasar jets or jet-linked enhanced coronae (e.g., [Zhu et al. 2020, 2021](#)).

The photometric properties used in the sample selection are listed in Table 1.

2.2. Chandra observation and data reduction

We performed Chandra snapshot observations of the selected eight quasars with large C IV EWs. Chandra ACIS is the ideal instrument to carry out these observations due to its high sensitivity and low background, compared to *XMM-Newton*, for snapshot point-source observations. The exposure times of our targets range from 2.8 to 6.0 ks. The observation details are summarized in Table 2.

We used standard CIAO tools to reduce our X-ray data, following the procedures described in section 3 of T20. After the `chandra_repro` processing, we extracted a light curve, and then used the `deflare` tool to remove any time intervals with background flares above the 3σ level in the light curve. Then we employed the `fluximage` tool to generate images and exposure maps for both the soft (0.5–2 keV) and hard (2–7 keV) bands. After the images were created, `wavdetect` was run on each image to search for sources. For each detected source, we compared the positions from `wavdetect` with the SDSS coordinates, and if the coordinates of a detected source in either band matched within $0.5''$ of the SDSS position, we adopted this coordinate as the source position. Around this position, we use `srcflux` to create a circular region that encloses 90% of the PSF at 1.0 keV, and then we extracted the raw counts within the circular region with the radius plus 5 additional pixels (e.g., [Gibson et al. 2008](#)). The background was extracted in an annulus with radius equal to the source radius plus 15 (50) pixels for the inner (outer) radius. For J103312.84+110555.3 there is another faint source in the hard band in the background region, and we removed it manually. We visually inspected our source and background regions and verified that there are no other apparent extraneous sources in these regions. We calculated the 1σ errors of the net counts, based on the Poisson errors on the extracted source and background counts ([Gehrels 1986](#)). The effective exposure time corrected for vignetting in both the source and background regions can be derived from the exposure maps. Finally,

we used the `specextract` tool to create the source and background spectra.

As in T20, we computed the band ratios (i.e., the ratio of the hard-band to soft-band counts) with uncertainties using the Bayesian Estimation of Hardness Ratio (BEHR; [Park et al. 2006](#)) package. To compare with the T20 quasar sample, we first used the same method as theirs to estimate the effective power-law photon index (Γ_{eff}), i.e., using the `modelflux` tool, given the instrumental responses and a model of a power-law with Galactic absorption. We minimized the difference between the measured hard-band count rate and the prediction from the soft-band count rate and a series of Γ using `modelflux` to determine Γ_{eff} . We then estimate the rest-frame flux density at 2 keV, $f_{2\text{keV}}$, using Γ_{eff} and the measured soft-band count rate. We deduced the upper and lower limits for $f_{2\text{keV}}$ by moving count rates in the soft and hard bands in turn both upward and downward by the error and repeating the process above. Additionally, given the relatively high X-ray counts of our quasars (the median number of counts in the 0.5–7 keV band is 47 with a range of 16–67), we could also use XSPEC to fit the spectra with the same model to determine Γ_{eff} , and the fitting results agree well with the estimations from `modelflux`. Thus, we can use the XSPEC results for our quasars, which are more accurate, to compare with the `modelflux` results for the T20 sample. The X-ray properties are reported in Table 2.

2.3. Fitting optical spectra

We fitted all available SDSS spectra of the large C IV EW quasars, which are shown in Figure 1b, including the two from the T20 quasar sample. We measured the C IV EW using the method outlined in T20, so that we can consistently compare the C IV line properties of our quasars with the large quasar sample in T20. We employed the PyQSOFit⁶ ([Guo et al. 2018](#)) software, which is based on the code used in [Shen et al. \(2011\)](#). We first fitted the global continuum using a combination of a simple power-law, a low-order polynomial, and UV Fe II templates. The line-free regions (at rest-frame wavelengths) are built into PyQSOFit. Next we measured the properties of the C IV emission line. We fit a local power-law continuum to the rest-frame relatively line-free regions of 1445–1465 Å and 1690–1705 Å. The fitted continuum was then subtracted from the C IV line region, and three broad Gaussian profiles were used to fit the emission line within 1500–1600 Å (see Figure 1a). We masked the 3σ outliers from the spectrum smoothed

⁵ The radio-loudness parameter is defined as the ratio between the 6 cm flux density and the 2500 Å flux density: $R = f_{6\text{cm}}/f_{2500}$ ([Richards et al. 2011](#)).

⁶ <https://github.com/legolason/PyQSOFit>

by a 20-pixel boxcar filter to reduce the impact of narrow absorption lines around the C IV line. PyQSOFit returned the EW based on the multi-Gaussian model, FWHM, peak wavelength, and other measurements of the C IV line.

Another high-ionization emission line, He II $\lambda 1640$, has also been used as a proxy for the amount of ionizing radiation in previous work. Our method of measuring the He II EW is the same as in Timlin et al. (2021) (hereafter T21), also aiming to compare our quasars with the quasar sample with He II measurements in T21. The local continuum in the He II emission-line region of each spectrum was determined by fitting a linear model to the median values in the continuum windows 1420–1460 Å and 1680–1700 Å, and the 3σ clipping method was also incorporated to remove the effects of any narrow spikes in these regions. The He II EW was then measured by directly integrating the continuum-normalized flux in the window 1620–1650 Å. This method measures the emission where He II dominates the spectrum. The He II lines in all of our quasar spectra are well detected. The measurement results for the C IV and He II lines are reported in Table 3.

2.4. Long-term light curves

Because the X-ray observations, SDSS spectroscopic observations, and SDSS photometric observations are not simultaneous, we should assess the possible effects of quasar variability when we conduct multi-wavelength data analyses. We generate long-term light curves to check if there are substantial changes in the luminosities of these quasars at the times of the SDSS spectroscopic and X-ray observations.

The light curves are shown in Figure 2, including SDSS, the Catalina Real-time Transient Survey (CRTS, Drake et al. 2009), and the Zwicky Transient Facility (ZTF, Bellm et al. 2019) photometric data, and the dates of SDSS spectroscopic observations and the Chandra observations are marked. To correct for different filter curves, we convolved the nearest SDSS spectra with the ZTF/CRTS/SDSS filter curves to obtain the magnitude corrections, and all optical data are then cross-calibrated to SDSS g -band (Yang et al. 2020). While the calibration is slight and reliable for ZTF data since its filter curves are similar to SDSS, the calibration for CRTS data is more difficult and may have large uncertainties because CRTS data are observed through a wide band with a resolving power of ~ 1 and thus variations of spectral shape can make substantial differences.

It can be seen from the light curves that the magnitudes of the quasars have not increased or decreased

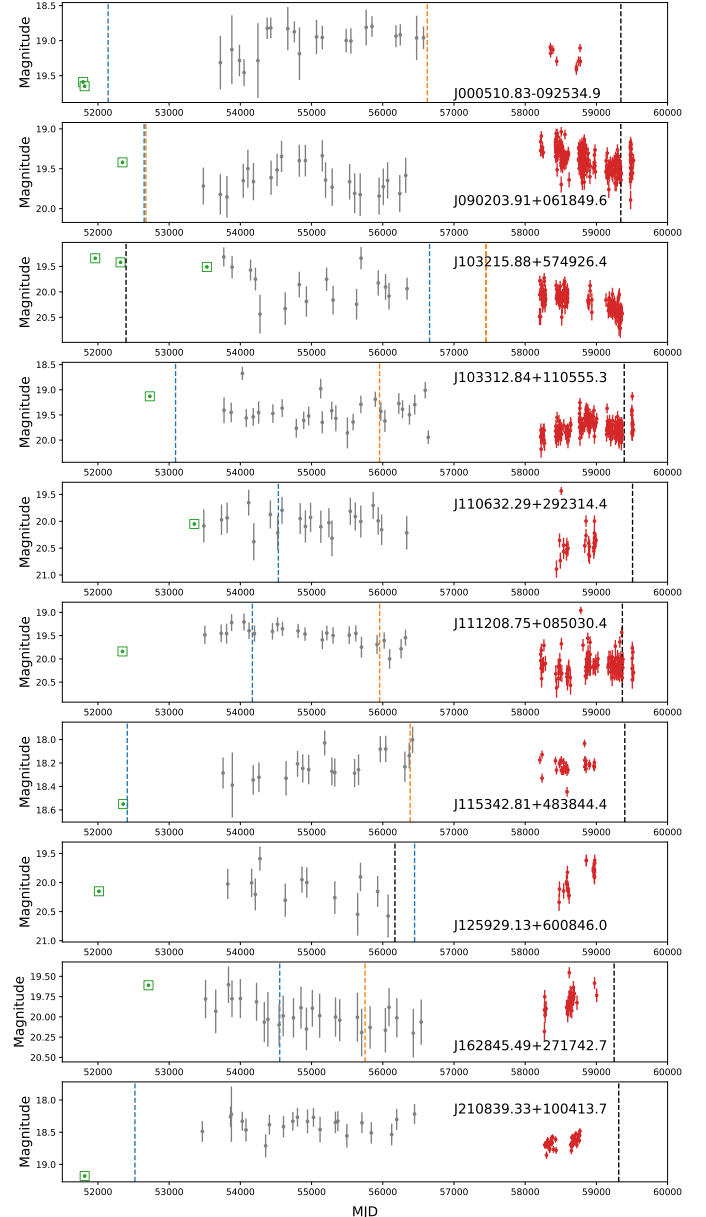


Figure 2. The long-term light curves and timelines of multi-wavelength observations. The light curves include SDSS (green points), CRTS (grey points) and ZTF (red points) photometric data, all cross-calibrated to SDSS g -band magnitude, and we marked the dates of SDSS spectroscopic observations (blue dashed lines for DR7 spectra, and orange for the others) and the Chandra observations (black dashed lines). The CRTS light curves are binned to reduce noise. To correct for different filter curves, we convolved the SDSS spectra with the ZTF/CRTS/SDSS filter curves to obtain the magnitude corrections.

substantially around the dates of the SDSS spectroscopic and X-ray observations. In addition, it has been suggested that single-epoch spectroscopic results do not significantly change where quasars are located in C IV

parameter space on rest-frame timescales of ≈ 300 days (Rivera et al. 2020). Therefore, we believe that quasar variability should not have material impacts upon the subsequent analyses.

In the multi-wavelength data analysis throughout the work, if not specified, we used the SDSS spectra and SDSS/ZTF photometric data closest to the X-ray observation dates to ensure as much consistency as possible between different bands.

3. BASIC OPTICAL/UV AND X-RAY OBSERVATIONAL RESULTS

3.1. Large emission-line EWs

It is well known that the emission-line EWs of quasars are related to their luminosities (the Baldwin effect; Baldwin 1977), i.e., the emission-line EW decreases with increasing continuum luminosity. Under our source-selection criteria in Section 2.1, the C IV EWs of our eight quasars generally are significantly larger than those of other quasars in T20 with similar UV luminosities (see Figure 3a). As mentioned in Section 2.1, only two quasars in T20 have similar L_{2500} values and C IV EWs, and their X-ray and optical properties are also similar to those of our new sample, which will be shown in the results below, and thus we included them in the following analyses. We fitted a linear relation between $\log(\text{C IV EW})$ and $\log(L_{2500})$ to the T20 C IV subsample of 637 typical quasars, together with our large C IV EW quasars.

We also compared the He II EWs of our quasars with the large He II EW sample in T21. The He II EWs of the T21 quasar sample are strongly related to L_{2500} , and our large C IV EW quasars also have large He II EWs (see Figure 3b), which further indicates a larger number of ionizing photons reaching the high-ionization broad emission-line region. For the $\log(\text{He II EW})$ – $\log(L_{2500})$ relation, we also used a linear relation to fit the 206-quasar sample from T21. Note that some of the He II EWs in T21 are upper limits, and thus throughout this work we used the Bayesian fitting method developed in Kelly (2007) and implemented in the `linmix`⁷ Python package, which can incorporate measurements that are upper (or lower) limits, including errors in both dimensions.

Even though our large C IV EW quasars improve the coverage in the above two parameter spaces, they are numerically overwhelmed by the 637 typical quasars in the T20 C IV subsample or the 206 in the T21 sample,

so that the best-fit linear models⁸ are almost identical to those obtained in T20 and T21 (see T20 Equation 8 and T21 Table 2), and other relations we derive below are in the same situation. Thus, the linear relations provide general trends for typical quasars that can be compared with our sample.

We also considered Mg II and C III], two low-ionization emission lines visible in the spectra, and compared their EWs with those of the T20 sample. Compared with the T20 sample, the Mg II EWs of our quasars are generally larger (see Figure 3c), while the C III] EWs show no significant difference (see Figure 3d). As mentioned in Section 2.4, except for the two quasars from the T20 sample, for the other eight quasars we use the latest SDSS spectra and ZTF photometric data in the analysis, namely the observation results closest in time to our X-ray observations.

3.2. X-ray excess

In addition to emission-line EWs, another commonly used indirect measurement of the strength of the ionizing emission in quasars is the optical/UV-to-X-ray power-law spectral slope, α_{ox} . We also plausibly expected our large C IV EW quasars to have larger α_{ox} than the predictions from the standard α_{ox} – L_{2500} relation (α_{ox} values are reported in Table 2.). The result was as expected (see Figure 4). We also depicted 32 WLQs from the Ni et al. (2018, 2022) “Representative” sample for comparison. It is notable that the WLQs are often X-ray weaker than what the α_{ox} –2500 Å relation predicts, while our large C IV EW quasars are generally X-ray stronger.

The X-ray excess can also be seen in the combined spectral energy distribution (SED) (see Figure 5). The IR-to-UV SED photometric data were from the Pâris et al. (2018) catalog. These data have been corrected for Galactic extinction following the dereddening approach of Cardelli et al. (1989) and O’Donnell (1994) and have been corrected for intergalactic medium extinction following Meiksin (2006). We compared this composite SED with the composite quasar SED of optically luminous quasars from Richards et al. (2006). The combined IR-to-UV SED of the large C IV EW quasars is similar to the composite quasar SED, but the X-ray emission shows an apparent excess. Note that the apparent SDSS u -band and g -band deviations are caused by the strong Ly α and C IV emission lines, which are estimated from the spectra to cause an excess of about 0.2 dex.

⁸ $\log_{10}(\text{C IV EW}) = (-0.220 \pm 0.018)\log_{10}(L_{2500}) + (8.392 \pm 0.555)$
and $\log_{10}(\text{He II EW}) = (-0.308 \pm 0.022)\log_{10}(L_{2500}) + (10.094 \pm 0.684)$

⁷ <https://linmix.readthedocs.io/en/latest/maths.html>

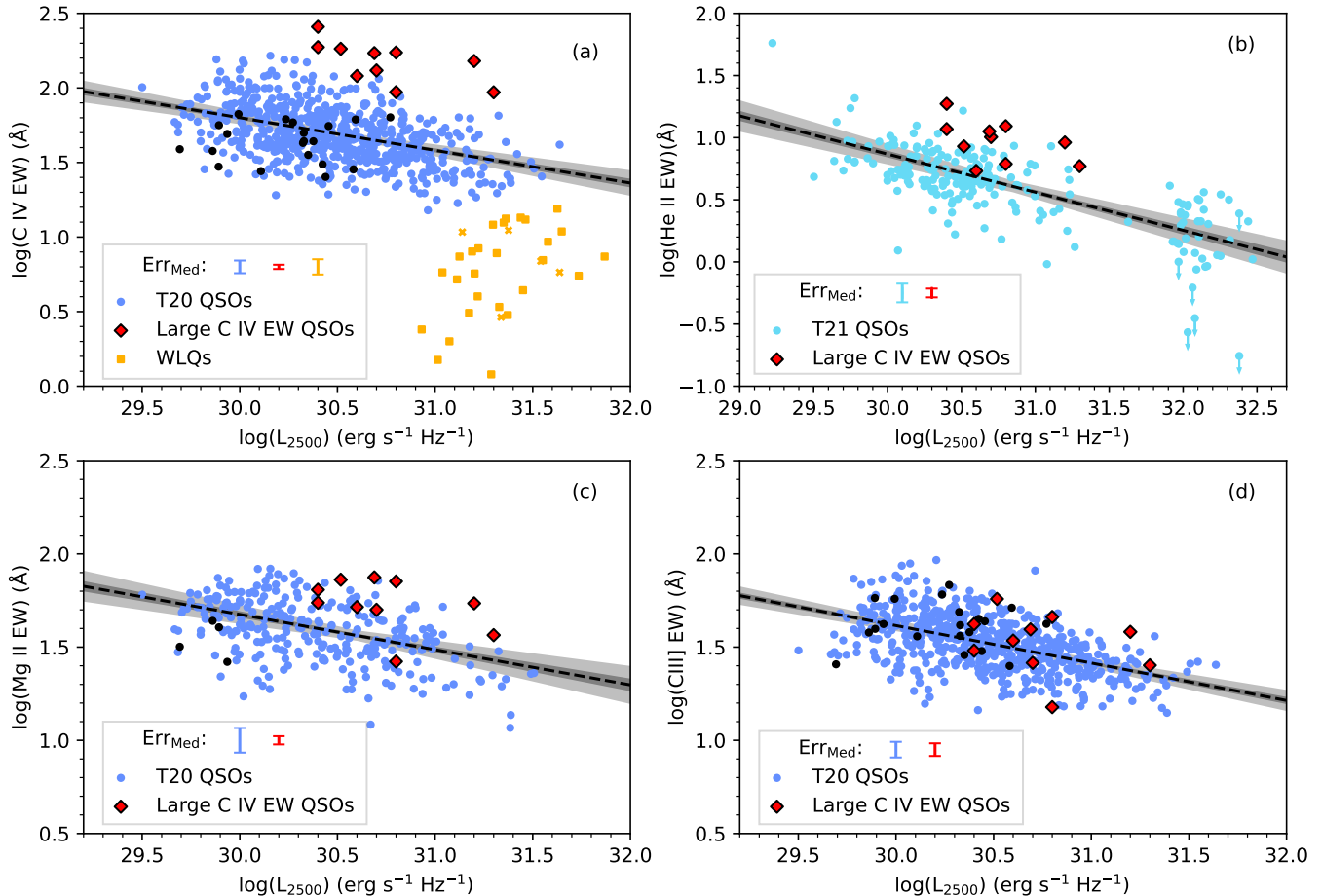


Figure 3. (a) The Baldwin effect (dashed black line; grey/dark grey shaded region depicts the $3\sigma/1\sigma$ confidence interval) derived using the 637 typical quasars in the T20 C IV subsample (blue points; black points represent quasars with X-ray upper limits) and the large C IV EW quasars (red diamonds). WLQs (orange squares; orange crosses indicate WLQs with X-ray upper limits) from the Ni et al. (2018, 2022) Representative sample are also included for comparison. The median errors on $\log(\text{C IV EW})$ of the three samples are represented by error bars in the corresponding colors (labeled as “Err_{Med}”), and the measurement error of L_{2500} is too small to be depicted. Clearly the WLQs and the large C IV EW quasars are extreme outliers from the general population in T20. (b) The Baldwin effect between $\log(\text{He II EW})$ and $\log(L_{2500})$ (dashed black line; grey/dark grey shaded region depicts the $3\sigma/1\sigma$ confidence interval); this relation is used to compute $\Delta\log(\text{He II EW})$. The light blue points are 206 quasars from the T21 He II sample, the downward-pointing arrows depict upper limits on the He II EW when the emission line is not detected, and the red diamonds are our large C IV EW quasars; their median errors on $\log(\text{He II EW})$ are indicated by the error bars. Larger He II EWs of the large C IV EW quasars also indicate a larger number of ionizing photons reaching the high-ionization broad emission-line region. (c,d) The same as panel (a), replacing C IV EW with Mg II EW and C III] EW.

Using the relations between α_{ox} , C IV EW, He II EW, and L_{2500} , respectively, we can derive the luminosity-adjusted values, $\Delta\alpha_{\text{ox}}$, $\Delta\log(\text{C IV EW})$ ⁹, and $\Delta\log(\text{He II EW})$. The $\Delta\alpha_{\text{ox}}$ values of our large C IV EW quasars are generally larger than the linear $\Delta\log(\text{C IV EW})-\Delta\alpha_{\text{ox}}$ relation prediction and perhaps also the $\Delta\log(\text{He II EW})-\Delta\alpha_{\text{ox}}$ relation prediction (see

Figure 6). The X-ray excess of the large C IV EW quasars in the $\Delta\log(\text{He II EW})-\Delta\alpha_{\text{ox}}$ space is not as large as in the $\Delta\log(\text{C IV EW})-\Delta\alpha_{\text{ox}}$ space, which is partly because of higher uncertainty in the He II EW measurements and thus a larger uncertainty of the derived correlation.

⁹ Like $\Delta\alpha_{\text{ox}}$, $\Delta\log(\text{C IV EW})$ is the luminosity-adjusted value defined as observed $\log(\text{C IV EW})$ minus the prediction from the $\log(\text{C IV EW})-L_{2500}$ relation in T20; $\Delta\log(\text{He II EW})$ is defined in the same way.

3.3. The C IV EW – C IV blueshift relation

We compared the large C IV EW quasars with T20 quasars and WLQs in the

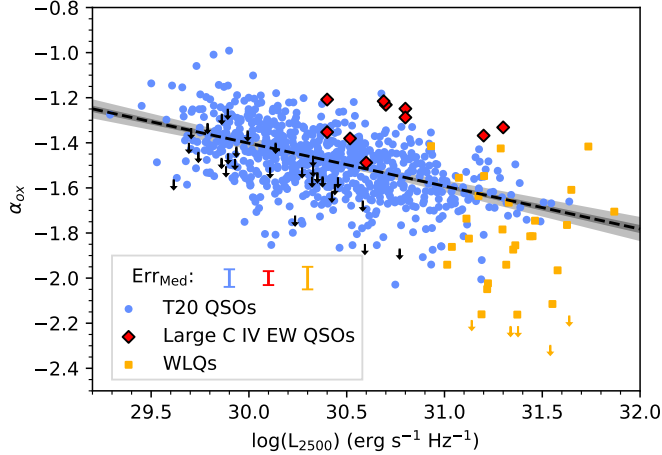


Figure 4. Dependence of α_{ox} on the 2500 Å monochromatic luminosity, L_{2500} . Blue points represent the “Sensitive” sample of 753 typical quasars in T20 and black arrows depict quasars with X-ray upper limits, red diamonds are our large C IV EW quasars, and orange squares and orange arrows represent WLQs and WLQs with X-ray upper limits; their median errors on α_{ox} are shown by error bars in the corresponding colors. The black dashed line depicts the best-fit relation between α_{ox} and $\log(L_{2500})$ and is used to compute $\Delta\alpha_{\text{ox}}$; the $3\sigma/1\sigma$ confidence interval is shown as the grey/dark grey shaded region. The WLQs are often X-ray weaker than what the $\alpha_{\text{ox}} - L_{2500}$ relation predicts while our large C IV EW quasars are generally X-ray stronger.

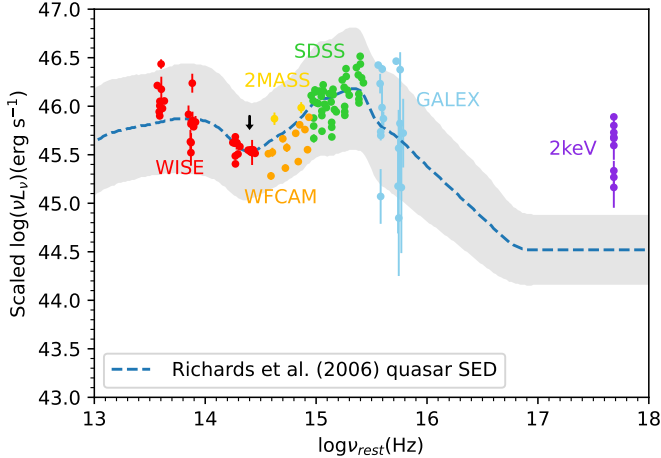


Figure 5. Combined SED for the large C IV EW quasars. The SED for each object was scaled to the composite quasar SED of optically luminous quasars (dashed line, and 1σ error shown with grey region; Richards et al. 2006) at rest-frame $10^{14.4}$ Hz (black arrow), and then combined. The combined IR-to-UV SED of the large C IV EW quasars is similar to the composite quasar SED, except for the apparent X-ray excess.

$\Delta\log(\text{C IV EW}) - \Delta(\text{C IV blueshift})^{10}$ space (see Figure 7). For quasars that have more than one SDSS spectral observation, we show the measurements of all spectra to inspect the impact of C IV variability on the position, and points of the same source are connected by dashed lines. The sizes of the points indicate the $\Delta\alpha_{\text{ox}}$ values. Our quasars (diamonds) occupy the upper-left corner of the space, meaning that they generally have larger C IV EW, smaller blueshifts ($\Delta(\text{C IV blueshift}) < 0$), and stronger X-ray emission compared to the T20 typical quasar sample. The C IV line variability does not change this trend (also see Rivera et al. 2020).

WLQs usually have small C IV EWs, large C IV blueshifts, and weak X-ray emission. In this sense, our large C IV EW quasars seem to be “anti-WLQs”, representing the “opposite” extreme from WLQs in Figure 7. Many properties of WLQs can be explained by a “shielding” model, in which a geometrically and optically thick inner accretion disk and its associated wind, expected for a quasar accreting at a high Eddington ratio, both prevents ionizing EUV/X-ray photons from reaching the high-ionization broad emission-line region and also sometimes blocks the line-of-sight to the central X-ray emitting region (e.g., Ni et al. 2018, 2022). Thus, WLQs have weak emission lines and often weak X-ray emission with signs of heavy intrinsic X-ray absorption. If the large C IV EW quasars represent the “opposite” extreme from WLQs, they might be expected to have relatively low Eddington ratios and little intrinsic absorption.

3.4. Assessing causes of the strong X-ray emission

To attempt to assess what causes the strong X-ray emission of the large C IV EW quasars, we tried to find clues from their X-ray spectra and Eddington ratios. We fitted the X-ray spectra using XSPEC again, adding an intrinsic absorption component to the model. The resulting hydrogen column densities are small ($N_{\text{H}} < 10^{22} \text{ cm}^{-2}$), just as we expected, so that intrinsic absorption effects are small, and the effective power-law photon indices (Γ_{eff}) provide an appropriate measure of the intrinsic spectral shape. No other distinctive features can be seen in the spectra, partly because of the limited counts, so that few clues about the X-ray excess can be obtained via X-ray spectral fitting. The median Γ_{eff} of the large C IV EW quasars is 1.81 ± 0.13 (the 1σ uncer-

¹⁰ We define the C IV blueshift as $c(1549.06 - \lambda_{\text{peak}})/1549.06$, measured in units of km s^{-1} , where λ_{peak} is the measured peak of the emission line (in Å), 1549.06 Å is the laboratory wavelength of the C IV emission line (see Table 4 of Vanden Berk et al. 2001), and c is the speed of light. See Table 3 for measured C IV blueshift values for all ten quasars.

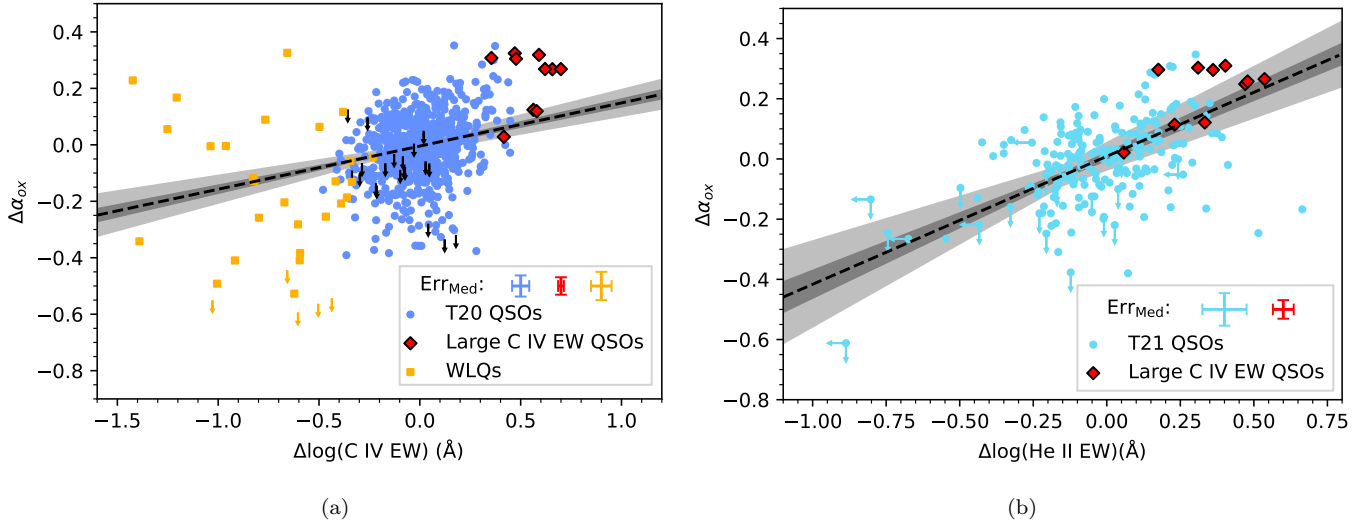


Figure 6. (a) The luminosity-adjusted α_{ox} , $\Delta\alpha_{\text{ox}}$, as a function of luminosity-adjusted C IV EW, $\Delta\log(\text{C IV EW})$; the color scheme is the same as in Figure 3, and the median error on $\Delta\alpha_{\text{ox}}$ and $\Delta\log(\text{C IV EW})$ of each sample is shown by the error bar in the corresponding colors. The general X-ray excess of our large C IV EW quasars is also apparent with respect to their $\Delta\log(\text{C IV EW})$, in broad accord with the scenario that extremely strong ionizing radiation leads to larger C IV EW in these quasars. (b) $\Delta\alpha_{\text{ox}}$ as a function of luminosity-adjusted He II EW, $\Delta\log(\text{He II EW})$. The light blue points are T21 quasars; left-pointing arrows depict upper limits of the $\Delta(\text{He II EW})$, and downward-pointing arrows depict upper limits of $\Delta\alpha_{\text{ox}}$ for X-ray non-detections. The red diamonds are our large C IV EW quasars. Error bars of $\Delta\alpha_{\text{ox}}$ and $\Delta\log(\text{He II EW})$ are shown in the bottom-right corner.

tainty is derived from bootstrap resampling), consistent with the median value of 1.9 for typical quasars (e.g., Scott et al. 2011). We also compared the distribution of their Γ_{eff} with those of the T20 quasars (Figure 8a), but they do not show a significant difference. We performed a two-sample Anderson-Darling test to quantify the difference, if any, between the two distributions, and the null-hypothesis probability is $P_{\text{null}} = 0.55$, meaning the Γ_{eff} values of our large C IV EW quasars are not demonstrably different from those of the T20 quasars. While any solid conclusions about the Γ_{eff} values of our targeted quasars must await higher quality X-ray spectra, we do note that our median Γ_{eff} of 1.81 ± 0.13 is consistent with fairly low Eddington ratios (e.g., Shemmer et al. 2008; Brightman et al. 2013).

It has been suggested that the 2–10 keV bolometric corrections (L_{bol}/L_X) of quasars are positively correlated with their Eddington ratios (e.g., Vasudevan & Fabian 2007; Lusso et al. 2012), and our large C IV EW quasars have low L_{bol}/L_X which might imply low Eddington ratios. Besides, if indeed WLQs have high Eddington ratios, then our apparent “anti-WLQs” may also have low Eddington ratios in this sense. Thus, we estimated the Eddington ratios of our large C IV EW quasars. We obtain bolometric luminosities (L_{bol}) of our targets via integrating the SED from 1 micron to 10 keV, and the multiwavelength photometric data come from

the Pâris et al. (2018) catalog (see Figure 5). The black-hole masses are from the Shen et al. (2011) catalog. All of our quasars have both C IV and Mg II in their spectra, and we only use black-hole masses estimated from Mg II FWHMs to avoid systematic discrepancies caused by different “single-epoch” black-hole mass estimation methods (e.g., Shen et al. 2008). The black-hole mass estimator is consistent in subsequent works (e.g., Shen & Liu 2012; Trakhtenbrot & Netzer 2012). The Eddington ratios are listed in Table 1 and shown in Figure 8b. We also plotted the distribution of Eddington ratios of the T20 quasars which have black-hole masses estimated from Mg II FWHMs (we directly use L_{bol} from the Shen et al. 2011 catalog for the T20 quasars, which are appropriate in an average sense). The Eddington ratios of our sample, with a median value of 0.11, are suggestively smaller than those of T20 quasars according to an Anderson-Darling test ($P_{\text{null}} = 0.007$). However, we note there are large uncertainties in Eddington-ratio estimation, especially in the black-hole mass measurements, and thus a larger sample is needed to draw a conclusion.

4. DISCUSSION

Above we have shown that luminous quasars selected to have the most extreme C IV EW are characterized by excess EW in He II and Mg II, but only marginal excess C III] EW (see Figure 3). In addition, there is clear

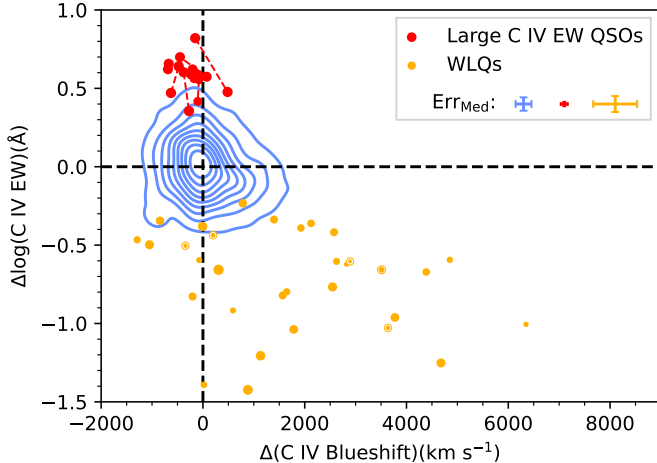


Figure 7. The $\Delta\log(\text{C IV EW})$ with respect to $\Delta(\text{C IV blueshift})$; both are luminosity-adjusted values. The blue contours depict the distribution of T20 quasars. Red points are our large C IV EW quasars, orange points represent WLQs, and WLQs with X-ray upper limits are circled; the sizes of the points indicate the $\Delta\alpha_{\text{ox}}$ values. All spectral observation results of the large C IV EW quasars are shown, and points of the same source are connected by dashed lines. The vertical and horizontal dashed lines represent the expected C IV blueshift and C IV EW according to L_{2500} . Median errors for T20 quasars, the large C IV EW quasars, and WLQs are shown by the error bars in the corresponding colors. Clearly our large C IV EW QSO sample has strong X-ray emission and small blueshift, representing the “opposite” extreme from the WLQs in this parameter space.

excess X-ray emission (see Figures 4–6). What is the physical mechanism driving these unusual properties? Possible solutions are described below.

The EW of the broad emission lines depends, among other things, on the covering factor of the broad line region gas. Are these high C IV EW AGN characterized by a very high covering factor? If so, then all lines should be enhanced by about the same factor. As described above, the C III] EW shows only a slight enhancement, if any, which clearly excludes this option.

Another way to enhance the C IV EW, without changing the broad line region covering factor, is by lowering the observed local continuum luminosity, without changing the continuum luminosity that illuminates the broad line region. If the optical-UV continuum in quasars is produced by an accretion disk, the observed luminosity is expected to be inclination dependent. Do high C IV EW quasars have a nearly edge-on and limb-darkened view? In this case as well, all UV lines should be enhanced in about a similar way. So, as noted above, this possibility is also excluded.

We clearly need a mechanism that selectively enhances the C IV EW. Another possible mechanism is an en-

hanced covering factor due to the addition of a low column density gas. If the gas ionization is matter bounded, rather than ionization bounded, it will produce only high-ionization lines. Such a component indeed characterizes the so-called “wind component” of the broad line region gas, characterized by a strong blueshift, and is seen clearly only in high-ionization lines, in particular in C IV. Such a component can explain the lack of significant lower ionization C III] emission. However, such a low-column component will not produce any Mg II emission. The observed significant enhancement of Mg II emission clearly excludes this mechanism.

Since the excess C IV EW is associated with excess X-ray emission, can the observed peculiar pattern of different UV line enhancements be explained by an ionizing continuum effect?

4.1. Comparison with photoionization calculation results

Below we show that the ionizing continuum shape can indeed explain a significant part of the observed trends, but that metallicity also plays a significant role, and its inclusion provides a nearly perfect explanation.

4.1.1. The effect of the ionizing continuum

We use the photoionization code Cloudy (Ferland et al. 1998), in the mode which includes the radiation pressure compression (RPC) effect. This mode includes both the energy and momentum transmitted to the gas by the incident photoionizing radiation which is absorbed. As a result the gas density is not a free parameter, and is also not uniform. The density structure within the photoionized slab is set by the absorbed radiation, and the resulting ionization structure is independent of distance from the ionizing source. The remaining free parameters are the spectral hardness of the ionizing continuum and the gas metallicity. We use the RPC solutions for gas in the broad line region as reported by Baskin et al. (2014); particularly, see their Figure 5.

Table 4, in its first row, reports the maximal EWs of the C IV, He II, Mg II, and C III] lines for a Solar metallicity ($Z = 1$) gas and a typical ionizing continuum slope (from 1000 Å to 1 keV) of $\alpha_{\text{ion}} = -1.6$, which corresponds to $\alpha_{\text{ox}} = -1.45$. The second row reports the effect on the EWs of a harder ionizing continuum of $\alpha_{\text{ion}} = -1.2$, which corresponds to $\alpha_{\text{ox}} = -1.16$. The two model values of α_{ox} are comparable to the mean α_{ox} values of the typical quasar sample and our large C IV EW quasar sample.

The last row in Table 4 gives the observed EW enhancement, $\Delta\text{EW}/\text{EW}$, for each of the lines, which is

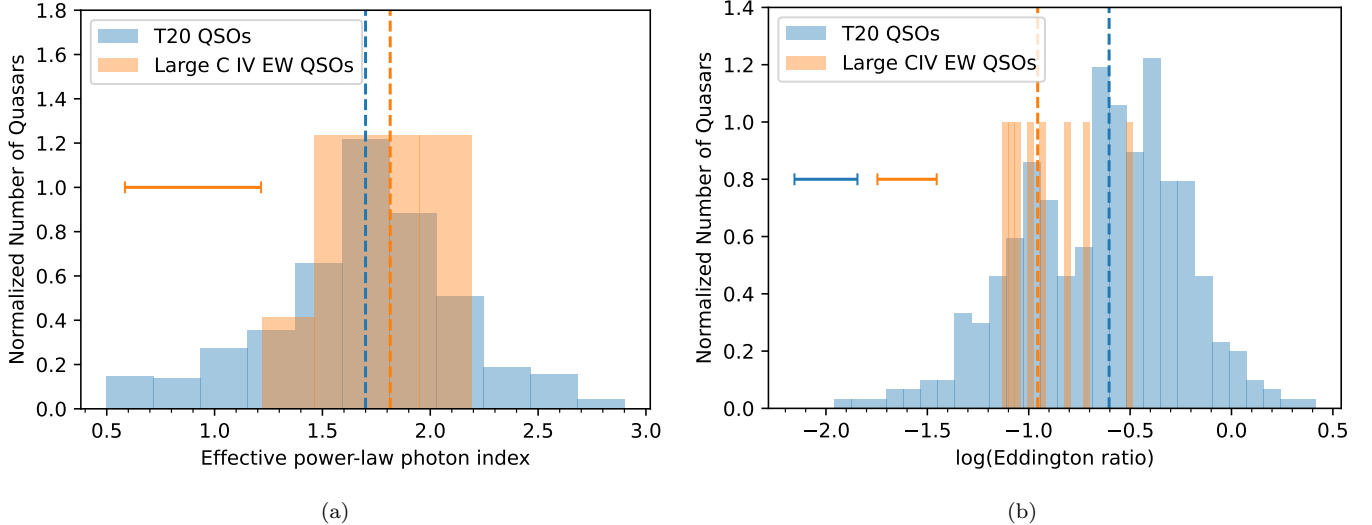


Figure 8. (a) The distribution of effective power-law photon indexes (Γ_{eff}) for T20 quasars and our large C IV EW quasars. The median Γ_{eff} values are shown by the vertical dashed lines in corresponding colors. The median error on Γ_{eff} of large C IV EW quasar sample, estimated from XSPEC, is shown with the error bar. The Γ_{eff} of our large C IV EW quasars do not deviate apparently from T20 typical quasars. (b) The distribution of $\log(\text{Eddington ratio})$ for T20 quasars and our large C IV EW quasars. The median $\log(\text{Eddington ratio})$ values are shown by the vertical dashed lines in corresponding colors. The median errors on $\log(\text{Eddington ratio})$ for both samples are shown with the error bars; note that these errors only included measurement uncertainties but not the statistical uncertainty from virial mass calibrations or the systematic uncertainties for the virial black-hole masses (Shen et al. 2011).

derived as follows. For each object we found ΔEW , that is observed EW minus expected EW from the Baldwin relation (the best-fit dashed line in Figure 3), and then calculate the mean fractional increase $\Delta\text{EW}/\text{expected EW}$. For the seven objects with more than one spectroscopic observation, the mean C IV EW obtained with the latest observation is 17% smaller than that obtained with earlier observations, so we corrected the C IV EW of the other three objects by a factor of 0.83 when calculating the mean fractional increase to account for this variability bias.

From rows 1 and 2, the C IV line EW increases by a factor of 2.6, which corresponds to $\Delta\text{EW}/\text{EW} = 1.6$, significantly lower than the observed $\Delta\text{EW}/\text{EW} = 2.33 \pm 0.14$. For the He II EW the predicted and observed $\Delta\text{EW}/\text{EW}$ match well, 1.31 versus 1.23 ± 0.22 . For the Mg II line the predicted $\Delta\text{EW}/\text{EW} = 1.35$ which is heavily offset from the observed value of 0.61 ± 0.10 . For C III] (which is inevitably blended with Si III]) the fit is marginal, with predicted 0.49 versus 0.2 ± 0.1 .

Thus, only the He II line enhancement is well explained by the observed level of excess hardness of the ionizing continuum. The observed C IV excess emission is significantly stronger than predicted, while the observed Mg II excess is significantly weaker than predicted. These mismatches become more pronounced in the C IV/Mg II line ratios (last column in Table 4). The

ratio is predicted to increase only by a factor of 1.11, that is an excess of 0.11 in the line ratio, while the average observed excess is 1.02 ± 0.16 (see also Figure 9). What physical mechanism makes the C IV/Mg II line ratio about twice as strong in very high C IV luminosity quasars?

4.1.2. The effect of the gas metallicity

Since the only two free parameters that affect the line strength are the shape of the ionizing continuum and the gas metallicity, we checked the effect of metallicity. The third line in Table 4 shows the EWs of the four lines for the mean ionizing continuum of $\alpha_{\text{ox}} = -1.45$ and sub-Solar metallicity of $Z = 0.5$ (see Figure 5 of Baskin et al. 2014). The C IV line is enhanced since it remains the main gas coolant, while the Mg II and the C III] lines become weaker since they are more minor coolants and the strength of such coolants depends on their ionic abundance. The He II EW is not affected by the lower Z value, as expected since this recombination line provides a rather clean measure of the shape of the ionizing continuum.

The large C IV EW quasars show a harder ionizing continuum, so we need to include the metallicity and the ionizing SED in the model calculations. In Baskin et al. (2014) the two effects are handled separately. We therefore assume the two effects are independent, and derive their combined effect by multiply-

ing their individual effects (rows 4 and 5 in Table 4). The 6th row shows the resulting predicted $\Delta\text{EW}/\text{EW}$ for the four lines. The large mismatch in the C IV and the Mg II EW excess now disappears. The low metallicity which enhances the C IV line, together with the harder continuum which also enhances the C IV line, gives a predicted $\Delta\text{EW}/\text{EW} = 2.14$ which matches well the observed value of 2.33 ± 0.14 . The strength of the Mg II line is reduced, leading to a predicted $\Delta\text{EW}/\text{EW} = 0.67$ which now matches well the observed value of 0.61 ± 0.10 . The C III] + Si III] blend is now reduced to $\Delta\text{EW}/\text{EW} = -0.10$, which remains marginally consistent with the observed value of 0.20 ± 0.10 . As noted above, the good match of the He II line remains unaffected by the reduced metallicity. The sub-Solar metallicity also provides a good match for the observed increase in the C IV / Mg II line ratio. The predicted excess in the line ratio is now 0.88, which matches well the observed mean excess of 1.02 ± 0.16 .

We therefore conclude that the observed specific pattern of the UV-line enhancements in the large C IV EW quasars is well explained by the combined effect of a hard ionizing continuum and sub-Solar metallicity.

The sub-Solar metallicity result is consistent with the interpretation that these objects lie at the extreme of low “eigenvector 1” (EV1) objects (Boroson & Green 1992), as indicated by their large C IV EW and excess red wing emission (see Figure 7). The opposite extreme, of extreme high EV1 objects, such as narrow-line Seyfert 1 galaxies, are generally characterized by high L/L_{Edd} (e.g., Boller et al. 1996; Laor 2000; Boroson 2002), and in addition are also characterized by high metallicity, as indicated by various UV-line ratios, such as C IV/N V and C IV/(Si IV+O IV) (Wills et al. 1999; Shemmer et al. 2004; Shin et al. 2013). This known trend supports the RPC photoionization results that the large C IV EW quasars, which show a sign of low L/L_{Edd} (see Figure 8b), have low, sub-Solar metallicity.

4.2. The nature of the unusually strong X-ray emission

Why are the large C IV EW quasars associated with excess X-ray emission? As described above, strong C IV emission is produced when the ionizing continuum is harder. Is the excess X-ray emission then just a selection effect? Or, is there a specific physical mechanism that enhances both the C IV and the X-ray emission?

A hint of a possible physical mechanism is provided by the rather strong correlation of $\Delta\alpha_{\text{ox}}$ and the C IV / Mg II line ratio (Figure 9). According to the RPC photoionization-model results, the effect of α_{ox} on the ratio C IV / Mg II is small. Specifically, the mean C IV EW / Mg II EW ratio of our sample is about 2.02 times

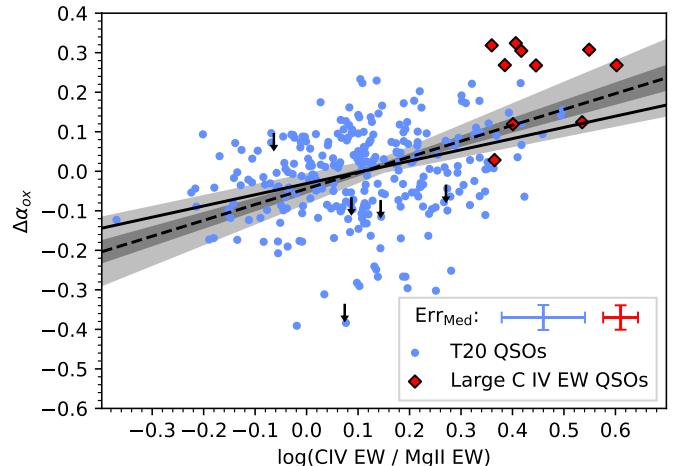


Figure 9. $\Delta\alpha_{\text{ox}}$ as a function of $\log(\text{C IV EW} / \text{Mg II EW})$. The color scheme is the same as in Figure 4, and the median error on $\Delta\alpha_{\text{ox}}$ and $\log(\text{C IV EW} / \text{Mg II EW})$ for each sample is shown by the error bars in the corresponding colors. The black solid line is the best-fit relation from T20. The dashed line and dark grey/grey regions are the linear relation and $1\sigma/3\sigma$ confidence intervals obtained by fitting the T20 sample and our large C IV EW quasar sample together, and the Spearman rank-order test statistic (ρ) and probability (P_{null}) are reported in the bottom left.

that of the T20 sample, while the model predicts that a change of $\Delta\alpha_{\text{ox}} = 0.3$ increases the ratio by a factor of 1.11 (Table 4), i.e. 0.05 dex, while the mean observed increase is 0.31 dex (Table 4). As discussed above, the higher C IV / Mg II in the strong C IV quasars is well explained by a low metallicity, specifically $Z = 0.5$. In fact, the distribution of C IV / Mg II values presented in Figure 9, including the extension of the T20 sample to low values, is well explained as a metallicity effect with a minor contribution from a changing SED. The derivation above (Table 4) gives a line-ratio enhancement by a factor of $\log(1.88) = 0.27$ for the harder ionizing continuum at low Z . Using the results in Baskin et al. (2014) we also derive that the high-metallicity $Z = 5$ models, with the softer ionizing continuum, decrease the line ratio by a factor of $\log(0.31) = -0.51$ from the general value. The observed mean line ratio of the entire quasar sample is $\log(1.42) = 0.15$, so the predicted range of values for $Z = 0.5-5$ is $\log(\text{C IV} / \text{Mg II}) = -0.36-0.42$, which matches well the observed range (Figure 9). This suggests that the C IV / Mg II ratio is a fairly clean measure of the metallicity.

Figure 9 then largely shows the effect of metallicity upon the X-ray emission. Why would higher metallicity make the coronal X-ray emission weaker? A possible answer is that higher metallicity leads to higher mass loss from the accretion disk, as expected for

radiation-pressure wind driving. The disk mass loss passes through the corona above the disk, leading to mass loading of the coronal gas, which increases the plasma cooling rate, making the corona cooler and thus lowering also the X-ray emission. The unusually low Z of the large C IV, extreme low EV1, quasars suppresses the wind, and as a result lowers the mass loading, which allows the formation of an effectively force-free magnetized plasma. The absence of mass loading may also allow a more highly magnetized corona, which may increase the heating rate due to reconnection events (Yuan et al. 2019a,b).

We note, in addition, that radio-quiet quasars with intrinsically strong X-ray emission are rare (e.g., Gibson et al. 2008; Pu et al. 2020). Using the large quasar sample in Pu et al. (2020), we estimate the fraction of X-ray strong quasars ($\Delta\alpha_{\text{ox}} > 0.2$) among radio-quiet quasars ($R < 10$) to be only 4 percent. Some studies have discussed the possibility that accretion-disk coronae contain the magnetic fields required for the launching of jets, and only when these magnetically dominated coronae are sufficiently strong can jets be launched (e.g., Merloni & Fabian 2002; Zhu et al. 2020). Under this scenario, some factor may have prevented the jet from launching, such as the topology of the magnetic field (e.g., Livio et al. 2003; Dexter et al. 2014), even though the coronal X-ray emission is strong. Theoretical studies have suggested that when external magnetic fields are too strong, an instability can develop that causes a jet to collapse, potentially forming a compact, collimated corona above the black hole (Yuan et al. 2019a,b). Thus, it is possible that our quasars failed to form jets even though their coronae are strong, which separates them from the X-ray strong, radio-loud quasars.

5. SUMMARY AND FUTURE WORK

In this work, we selected eight luminous quasars from the Shen et al. (2011) quasar catalog which have C IV EW $\geq 150 \text{ \AA}$ and performed Chandra snapshot observations of them. We studied the optical/UV and X-ray properties of these large C IV EW quasars and compared them to the large samples of typical quasars in T20 and T21. The main results are summarized below:

- (i) We fit the optical spectra of the eight target quasars and find they have large C IV EW excess, moderate He II EW and Mg II EW excess, and almost no C III] EW excess compared to the T20 or T21 typical quasars with similar UV luminosities. We also added two quasars from the T20 sample to our large C IV EW sample since they have similar C IV EWs and UV luminosities. See Section 3.1.

- (ii) These large C IV EW quasars have larger α_{ox} than the predictions from the $\alpha_{\text{ox}}-L_{2500}$ relation, which is as expected since both $\Delta\alpha_{\text{ox}}$ and the high-ionization emission lines can indicate the amount of ionizing radiation. The α_{ox} values of our ten quasars are also larger than expected from extrapolation of both the $\Delta\log(\text{C IV EW})-\Delta\alpha_{\text{ox}}$ and $\Delta\log(\text{He II EW})-\Delta\alpha_{\text{ox}}$ relations derived for typical quasars (see Figure 6). See Section 3.2.
- (iii) Our targets' C IV blueshifts are slightly smaller than for the T20 quasars with similar UV luminosities, making them locate at one extreme of the quasar locus in the C IV parameter space, opposite to WLQs. See Section 3.3.
- (iv) We investigated if the cause of the strong X-ray emission can be revealed by our targets' X-ray spectra or Eddington ratios. The intrinsic absorption is small, and the median Γ_{eff} is consistent with the median value for typical quasars. The Eddington ratios of these quasars are suggestively smaller than those of the T20 quasars. See Section 3.4.
- (v) The observed He II EW increase for our quasars agrees well with the RPC prediction for a harder ionizing continuum which matches the observed higher α_{ox} . This RPC model under-predicts the increase in C IV, and over-predicts the increase in Mg II. See Section 4.1.1.
- (vi) The RPC model for a harder ionizing continuum and sub-Solar ($Z = 0.5$) metallicity gas reproduces well the observed enhancement pattern of C IV, He II, Mg II, and C III] EWs. See Section 4.1.2.
- (vii) We find that the C IV/Mg II line ratio, in our sample and the T20 sample, is significantly correlated with $\Delta\alpha_{\text{ox}}$ for quasars in general. In addition, the RPC model results indicate this line ratio is mostly set by the gas metallicity and is nearly independent of the hardness of the ionizing continuum. A correlation of $\Delta\alpha_{\text{ox}}$ with gas metallicity is consistent with the known results that objects at the opposite extreme of EV1, extremely high EV1 objects, are characterized by both weak X-ray emission and high metallicity gas. See Section 4.2.
- (viii) The underlying physical mechanism which links the gas metallicity and the coronal X-ray emission is not known. A possible mechanism may be related to mass loading of the magnetized coronal gas. High gas metallicity may enhance radiation-pressure driven accretion-disk winds and thereby

mass loading of the corona, decreasing coronal X-ray emission. See Section 4.2.

There are several ways this work could be extended. The large C IV EW quasars apparently deviate from extrapolations of typical-quasar relations in some parameter spaces, but we need a larger sample to examine this behavior further. In addition, it would be valuable to obtain rest-frame optical-NUV spectra of these quasars to investigate further links between the UV-X-ray continuum and other optical emission lines like the Balmer lines. Simultaneous and repeated observations of X-ray and UV-to-optical spectra would be helpful to reveal the variation of X-ray emission and emission-line properties, and higher-quality X-ray spectra are also needed to better measure Γ values and thereby assess Eddington ratios.

We thank the referee for a constructive review. WNB and FZ acknowledge support from Chandra X-ray Center grant GO0-21080X and Penn State ACIS Instrument Team Contract SV4-74018 (issued by the Chandra X-ray Center, which is operated by the Smithsonian Astrophysical Observatory for and on behalf of NASA under contract NAS8-03060). AL acknowledges support by the Israel Science Foundation (grant no. 1008/18). QN acknowledges support from a UKRI Future Leaders Fellowship (grant code: MR/T020989/1). YQX acknowledges support from NSFC grants (12025303 and 11890693), the K.C. Wong Education Foundation, and the science research grants from the China Manned Space Project with NO. CMS-CSST-2021-A06.

The Chandra ACIS Team Guaranteed Time Observations (GTO) utilized were selected by the ACIS Instrument Principal Investigator, Gordon P. Garmire, currently of the Huntingdon Institute for X-ray Astronomy, LLC, which is under contract to the Smithsonian Astrophysical Observatory via Contract SV2-82024.

REFERENCES

- Baldwin, J. A. 1977, *ApJ*, 214, 679, doi: [10.1086/155294](https://doi.org/10.1086/155294)
- Baskin, A., & Laor, A. 2004, *MNRAS*, 350, L31, doi: [10.1111/j.1365-2966.2004.07833.x](https://doi.org/10.1111/j.1365-2966.2004.07833.x)
- Baskin, A., Laor, A., & Stern, J. 2014, *MNRAS*, 438, 604, doi: [10.1093/mnras/stt2230](https://doi.org/10.1093/mnras/stt2230)
- Becker, R. H., White, R. L., & Helfand, D. J. 1995, *ApJ*, 450, 559, doi: [10.1086/176166](https://doi.org/10.1086/176166)
- Bellm, E. C., Kulkarni, S. R., Graham, M. J., et al. 2019, *PASP*, 131, 018002, doi: [10.1088/1538-3873/aaecbe](https://doi.org/10.1088/1538-3873/aaecbe)
- Boller, T., Brandt, W. N., & Fink, H. 1996, *A&A*, 305, 53. <https://arxiv.org/abs/astro-ph/9504093>
- Boroson, T. A. 2002, *ApJ*, 565, 78, doi: [10.1086/324486](https://doi.org/10.1086/324486)
- Boroson, T. A., & Green, R. F. 1992, *ApJS*, 80, 109, doi: [10.1086/191661](https://doi.org/10.1086/191661)
- Brightman, M., Silverman, J. D., Mainieri, V., et al. 2013, *MNRAS*, 433, 2485, doi: [10.1093/mnras/stt920](https://doi.org/10.1093/mnras/stt920)
- Cardelli, J. A., Clayton, G. C., & Mathis, J. S. 1989, *ApJ*, 345, 245, doi: [10.1086/167900](https://doi.org/10.1086/167900)
- Dexter, J., McKinney, J. C., Markoff, S., & Tchekhovskoy, A. 2014, *Monthly Notices of the Royal Astronomical Society*, 440, 2185, doi: [10.1093/mnras/stu581](https://doi.org/10.1093/mnras/stu581)
- Drake, A. J., Djorgovski, S. G., Mahabal, A., et al. 2009, *ApJ*, 696, 870, doi: [10.1088/0004-637X/696/1/870](https://doi.org/10.1088/0004-637X/696/1/870)
- Ferland, G. J., Korista, K. T., Verner, D. A., et al. 1998, *PASP*, 110, 761, doi: [10.1086/316190](https://doi.org/10.1086/316190)
- Gehrels, N. 1986, *The Astrophysical Journal*, 303, 336. <http://adsabs.harvard.edu/abs/1986ApJ...303..336G>
- Gibson, R. R., Brandt, W. N., & Schneider, D. P. 2008, *ApJ*, 685, 773, doi: [10.1086/590403](https://doi.org/10.1086/590403)
- Green, P. J. 1998, *ApJ*, 498, 170, doi: [10.1086/305537](https://doi.org/10.1086/305537)
- Guo, H., Shen, Y., & Wang, S. 2018, PyQSOFit: Python code to fit the spectrum of quasars. <http://ascl.net/1809.008>
- Hewett, P. C., & Wild, V. 2010, *Monthly Notices of the Royal Astronomical Society*, 405, 2302, doi: [10.1111/j.1365-2966.2010.16648.x](https://doi.org/10.1111/j.1365-2966.2010.16648.x)
- Just, D. W., Brandt, W. N., Shemmer, O., et al. 2007, *ApJ*, 665, 1004, doi: [10.1086/519990](https://doi.org/10.1086/519990)
- Kelly, B. C. 2007, *ApJ*, 665, 1489, doi: [10.1086/519947](https://doi.org/10.1086/519947)
- Laor, A. 2000, *NewAR*, 44, 503, doi: [10.1016/S1387-6473\(00\)00088-9](https://doi.org/10.1016/S1387-6473(00)00088-9)
- Livio, M., Pringle, J. E., & King, A. R. 2003, *The Astrophysical Journal*, 593, 184, doi: [10.1086/375872](https://doi.org/10.1086/375872)
- Luo, B., Brandt, W. N., Hall, P. B., et al. 2015, *ApJ*, 805, 122, doi: [10.1088/0004-637X/805/2/122](https://doi.org/10.1088/0004-637X/805/2/122)
- Lusso, E., Comastri, A., Simmons, B. D., et al. 2012, *Monthly Notices of the Royal Astronomical Society*, 425, 623, doi: [10.1111/j.1365-2966.2012.21513.x](https://doi.org/10.1111/j.1365-2966.2012.21513.x)

Table 1. Photometric and Spectroscopic Properties of Large C IV EW Quasars

Object Name	RA	Dec	Redshift	$M_i(z=2)$	$\log L_{2500}$	$\Delta(g-i)$	R	$\log L_{\text{bol}}$	L/L_{Edd}
(J2000)	(deg)	(deg)							
(1)	(2)	(3)	(4)	(5)	(6)	(7)	(8)	(9)	(10)
Chandra snapshot observed quasars									
000510.83 – 092534.9	1.295151	–9.426368	1.866	–26.45	30.74	0.14	< 2.88	46.67 ± 0.02	0.085 ± 0.073
090203.91 + 061849.6	135.516296	6.313801	1.726	–26.33	30.69	–0.03	< 2.71	46.69 ± 0.02	0.121 ± 0.034
103312.84 + 110555.3	158.303513	11.098698	2.149	–27.08	30.99	–0.20	< 2.15	46.81 ± 0.06	0.101 ± 0.035
110632.29 + 292314.4	166.634537	29.387356	1.948	–25.77	30.47	–0.12	< 5.23	46.55 ± 0.04	0.074 ± 0.040
111208.75 + 085030.4	168.036484	8.841791	1.875	–26.05	30.58	–0.12	< 4.04	46.73 ± 0.02	0.194 ± 0.110
115342.81 + 483844.4	178.428391	48.645687	2.034	–27.46	31.14	0.02	< 1.25	47.06 ± 0.02	0.161 ± 0.078
162845.49 + 271742.7	247.189545	27.295200	1.961	–26.44	30.73	–0.10	< 2.99	46.69 ± 0.03	0.325 ± 0.061
210839.33 + 100413.7	317.163910	10.070496	2.154	–27.02	30.97	0.03	< 2.08	46.92 ± 0.05	0.082 ± 0.035
T20 quasars									
103215.88 + 574926.4	158.066179	57.824016	1.835	–26.32	30.69	0.01	< 3.90	46.58 ± 0.02	...
125929.13 + 600846.0	194.871400	60.146117	1.869	–25.89	30.52	0.15	< 4.83	46.53 ± 0.06	...

NOTE—Col.(1): Object name in the J2000 coordinate format. Cols.(2)–(3): The SDSS position in decimal degrees. Col.(4): Redshift adopted from Hewett & Wild (2010). Col.(5): Absolute i -band magnitude (corrected to $z = 2$; Richards et al. 2006). Col.(6): Logarithm of the rest-frame 2500 Å monochromatic luminosity in units of $\text{erg s}^{-1} \text{Hz}^{-1}$. Col.(7): Relative SDSS $g - i$ color. Col.(8): Radio-loudness parameter. Col.(9) Logarithm of the bolometric luminosities (erg s^{-1}) obtained through SED fitting (see Section 3.4). Col.(10) Eddington ratio (see Section 3.4).

Table 2. Chandra Observations and Photometric Properties of Large C IV EW Quasars

Object Name	ID	Date	Exposure Time	Count Rate	H/S	Γ_{eff}	$f_{2\text{keV}}$	$\log L_X$	α_{ox}	$\Delta\alpha_{\text{ox}}$
(J2000)			(ks)	(0.5–7 keV)				(2–10 keV)		
(1)	(2)	(3)	(4)	(5)	(6)	(7)	(8)	(9)	(10)	(11)
Chandra snapshot observed quasars										
000510.83 – 092534.9	24718	2021 May 10	3.969	12.0 $^{+3.0}_{-2.5}$	0.66 $^{+0.24}_{-0.18}$	2.15 ± 0.36	4.24 $^{+0.60}_{-0.54}$	45.41 $^{+0.12}_{-0.13}$	–1.22 $^{+0.02}_{-0.02}$	0.32 $^{+0.02}_{-0.02}$
090203.91 + 061849.6	24721	2021 Mar 9	2.896	5.4 $^{+2.8}_{-2.0}$	1.60 $^{+1.23}_{-0.70}$	1.22 ± 0.76	0.76 $^{+0.42}_{-0.32}$	44.93 $^{+0.17}_{-0.18}$	–1.51 $^{+0.07}_{-0.09}$	0.02 $^{+0.07}_{-0.09}$
103312.84 + 110555.3	24715	2021 Jun 26	4.356	10.3 $^{+2.7}_{-2.2}$	0.87 $^{+0.32}_{-0.23}$	1.62 ± 0.32	2.87 $^{+0.43}_{-0.58}$	45.47 $^{+0.11}_{-0.11}$	–1.34 $^{+0.02}_{-0.04}$	0.25 $^{+0.02}_{-0.04}$
110632.29 + 292314.4	24716	2021 Oct 21	5.720	4.1 $^{+1.6}_{-1.2}$	1.18 $^{+0.63}_{-0.43}$	1.63 ± 0.41	0.79 $^{+0.31}_{-0.23}$	44.93 $^{+0.14}_{-0.15}$	–1.38 $^{+0.05}_{-0.06}$	0.11 $^{+0.05}_{-0.06}$
111208.75 + 085030.4	24717	2021 May 31	4.065	12.0 $^{+3.0}_{-2.4}$	1.22 $^{+0.43}_{-0.31}$	1.49 ± 0.31	1.96 $^{+0.51}_{-0.41}$	45.36 $^{+0.09}_{-0.10}$	–1.29 $^{+0.04}_{-0.04}$	0.23 $^{+0.04}_{-0.04}$
115342.81 + 483844.4	24722	2021 Jul 4	2.799	23.9 $^{+4.9}_{-4.2}$	0.86 $^{+0.23}_{-0.20}$	1.95 ± 0.24	6.35 $^{+0.68}_{-1.05}$	45.78 $^{+0.09}_{-0.09}$	–1.28 $^{+0.02}_{-0.03}$	0.34 $^{+0.02}_{-0.03}$
162845.49 + 271742.7	24719	2021 Feb 4	4.149	8.4 $^{+2.6}_{-2.0}$	0.75 $^{+0.31}_{-0.23}$	2.10 ± 0.32	2.70 $^{+0.50}_{-0.60}$	45.30 $^{+0.14}_{-0.14}$	–1.28 $^{+0.03}_{-0.04}$	0.26 $^{+0.03}_{-0.04}$
210839.33 + 100413.7	24720	2021 Apr 10	3.578	11.7 $^{+3.2}_{-2.6}$	0.83 $^{+0.31}_{-0.23}$	2.19 ± 0.39	3.73 $^{+0.58}_{-0.77}$	45.54 $^{+0.12}_{-0.12}$	–1.29 $^{+0.02}_{-0.04}$	0.30 $^{+0.02}_{-0.04}$
T20 quasars										
103215.88 + 574926.4	3344	2002 May 1	34.206	18.3 $^{+1.1}_{-1.0}$	0.34 $^{+0.04}_{-0.04}$	1.82 ± 0.07	4.05 $^{+0.20}_{-0.19}$	45.45 $^{+0.02}_{-0.02}$	–1.22 $^{+0.01}_{-0.01}$	0.32 $^{+0.01}_{-0.01}$
125929.13 + 600846.0	13382	2012 Sep 1	13.596	4.5 $^{+1.0}_{-0.8}$	0.60 $^{+0.18}_{-0.26}$	1.81 ± 0.22	0.98 $^{+0.19}_{-0.16}$	44.92 $^{+0.09}_{-0.08}$	–1.38 $^{+0.03}_{-0.03}$	0.12 $^{+0.03}_{-0.03}$

NOTE—Col.(1): Object name. Col.(2): Chandra observation ID. Col.(3): Chandra observation start date. Col.(4): Effective exposure time with background flares cleaned and vignetting corrected. Col.(5): Net count rate (10^{-3} s^{-1}). Col.(6): Ratio of the hard-band (2–7 keV) and soft-band (0.5–2 keV) counts. Col.(7): Effective power-law photon index in the 0.5–7 keV band estimated using XSPEC. Col.(8): Flux density at rest-frame 2 keV in units of $10^{-31} \text{ erg cm}^{-2} \text{ s}^{-1} \text{ Hz}^{-1}$. Col.(9): Logarithm of the rest-frame 2–10 keV luminosity in units of erg s^{-1} , derived from Γ_{eff} and the observed-frame 2–7 keV flux. Col.(10): Observed α_{ox} . Col.(11): The luminosity-adjusted α_{ox} , $\Delta\alpha_{\text{ox}}$.

Table 3. Optical Spectral Fitting Results for Large C IV EW Quasars

Object Name (J2000)	MJD	C IV EW (\AA)	C IV peak (\AA)	C IV blueshift (km s^{-1})	He II EW (\AA)
(1)	(2)	(3)	(4)	(5)	(6)
Chandra snapshot observed quasars					
000510.83 – 092534.9	52143 56625	158.20 \pm 7.05 93.69 \pm 4.19	1547.48 \pm 0.34 1547.13 \pm 0.21	305.52 \pm 65.07 374.40 \pm 41.39	7.58 \pm 1.34 6.14 \pm 0.42
090203.91 + 061849.6	52649 52674	157.50 \pm 8.11 120.25 \pm 4.31	1546.43 \pm 0.33 1546.78 \pm 0.45	509.60 \pm 63.17 440.57 \pm 87.46	9.09 \pm 1.41 5.40 \pm 1.47
103312.84 + 110555.3	53090 55955	232.84 \pm 9.68 130.98 \pm 3.87	1544.55 \pm 0.81 1543.48 \pm 0.45	872.82 \pm 157.20 1079.18 \pm 87.01	13.16 \pm 1.68 10.12 \pm 0.79
110632.29 + 292314.4	54534	187.72 \pm 4.92	1547.70 \pm 0.25	263.93 \pm 48.27	11.72 \pm 1.21
111208.75 + 085030.4	54169 55956	179.14 \pm 5.15 256.91 \pm 7.49	1548.07 \pm 0.36 1549.14 \pm 0.79	192.39 \pm 69.36 –14.62 \pm 152.55	11.32 \pm 0.87 18.70 \pm 1.18
115342.81 + 483844.4	52412 56385	150.33 \pm 5.19 93.45 \pm 0.57	1547.59 \pm 0.24 1547.59 \pm 0.16	284.87 \pm 45.70 284.87 \pm 31.570	10.09 \pm 1.12 5.89 \pm 0.32
162845.49 + 271742.7	54553 55751	164.87 \pm 11.48 172.81 \pm 10.67	1546.41 \pm 0.36 1546.76 \pm 0.31	513.72 \pm 69.27 444.87 \pm 60.10	10.61 \pm 1.87 12.36 \pm 1.05
210839.33 + 100413.7	52520	151.50 \pm 4.60	1548.09 \pm 0.40	187.05 \pm 76.85	9.15 \pm 1.24
T20 quasars					
103215.88 + 574926.4	56657 57448 57452	162.25 \pm 4.26 207.07 \pm 12.08 172.76 \pm 6.90	1546.85 \pm 5.39 1548.63 \pm 3.67 1551.84 \pm 2.70	428.60 \pm 1042.81 83.77 \pm 711.20 –537.98 \pm 522.60	11.23 \pm 0.81 15.29 \pm 1.47 12.07 \pm 1.30
125929.13 + 600846.0	56447	191.14 \pm 10.64	1546.71 \pm 0.40	455.58 \pm 78.28	8.51 \pm 1.37

NOTE—Col.(1): Object name. Col.(2) Modified Julian date of the SDSS observations. Col.(3) Rest-frame equivalent width of the C IV broad emission line measured from the Gaussian models. Col.(4) Measured rest-frame peak of the C IV broad emission line. Col.(5) C IV emission line blueshift. Col.(6) Rest-frame equivalent width of the He II emission line.

Table 4. Comparison of RPC Model Predictions and Observations

	C IV	He II	Mg II	C III] (C III]+Si III)]	C IV/Mg II
EW _{Z=1,α=-1.6}	53	7.4	22.5	14 (21.4)	2.36
EW _{Z=1,α=-1.2}	138	17.1	52.8	18 (31.8)	2.61
EW _{Z=0.5,α=-1.6}	64	7.4	16	8.3 (12.9)	4.00
EW _{Z=1,α=-1.2} /EW _{Z=1,α=-1.6}	2.60	2.31	2.35	1.29 (1.49)	1.11
EW _{Z=0.5,α=-1.6} /EW _{Z=1,α=-1.6}	1.21	1.00	0.71	0.59 (0.60)	1.70
(EW _{Z=0.5,α=-1.2} –EW _{Z=1,α=-1.6})/EW _{Z=1,α=-1.6} ^a	2.14	1.31	0.67	–0.24 (–0.10)	0.88
Observed $\Delta\text{EW}/\text{EW}$	2.33 \pm 0.14	1.23 \pm 0.22	0.61 \pm 0.10	0.20 \pm 0.10	1.02 \pm 0.16

NOTE—^aEW_{Z=0.5,α=-1.2}/EW_{Z=1,α=-1.6} is estimated by directly multiplying the factors in the 4th and 5th rows.

- Marlar, A., Shemmer, O., Anderson, S. F., et al. 2018, *ApJ*, 865, 92, doi: [10.3847/1538-4357/aad812](https://doi.org/10.3847/1538-4357/aad812)
- Meiksin, A. 2006, *Monthly Notices of the Royal Astronomical Society*, 365, 807, doi: [10.1111/j.1365-2966.2005.09756.x](https://doi.org/10.1111/j.1365-2966.2005.09756.x)
- Merloni, A., & Fabian, A. C. 2002, *Monthly Notices of the Royal Astronomical Society*, 332, 165, doi: [10.1046/j.1365-8711.2002.05288.x](https://doi.org/10.1046/j.1365-8711.2002.05288.x)
- Ni, Q., Brandt, W. N., Luo, B., et al. 2018, *MNRAS*, 480, 5184, doi: [10.1093/mnras/sty1989](https://doi.org/10.1093/mnras/sty1989)
- . 2022, *MNRAS*, 511, 5251, doi: [10.1093/mnras/stac394](https://doi.org/10.1093/mnras/stac394)
- O'Donnell, J. E. 1994, *ApJ*, 422, 158, doi: [10.1086/173713](https://doi.org/10.1086/173713)
- Pâris, I., Petitjean, P., Aubourg, É., et al. 2018, *A&A*, 613, A51, doi: [10.1051/0004-6361/201732445](https://doi.org/10.1051/0004-6361/201732445)
- Park, T., Kashyap, V. L., Siemiginowska, A., et al. 2006, *The Astrophysical Journal*, 652, 610, doi: [10.1086/507406](https://doi.org/10.1086/507406)
- Pu, X., Luo, B., Brandt, W. N., et al. 2020, *ApJ*, 900, 141, doi: [10.3847/1538-4357/abacc5](https://doi.org/10.3847/1538-4357/abacc5)
- Richards, G. T., Hall, P. B., Vand en Berk, D. E., et al. 2003, *AJ*, 126, 1131, doi: [10.1086/377014](https://doi.org/10.1086/377014)
- Richards, G. T., Strauss, M. A., Fan, X., et al. 2006, *The Astronomical Journal*, 131, 2766, doi: [10.1086/503559](https://doi.org/10.1086/503559)
- Richards, G. T., Kruczek, N. E., Gallagher, S. C., et al. 2011, *AJ*, 141, 167, doi: [10.1088/0004-6256/141/5/167](https://doi.org/10.1088/0004-6256/141/5/167)
- Rivera, A. B., Richards, G. T., Hewett, P. C., & Rankine, A. L. 2020, *ApJ*, 899, 96, doi: [10.3847/1538-4357/aba62c](https://doi.org/10.3847/1538-4357/aba62c)
- Scott, A. E., Stewart, G. C., Mateos, S., et al. 2011, *Monthly Notices of the Royal Astronomical Society*, 417, 992, doi: [10.1111/j.1365-2966.2011.19325.x](https://doi.org/10.1111/j.1365-2966.2011.19325.x)
- Shemmer, O., Brandt, W. N., Netzer, H., Maiolino, R., & Kaspi, S. 2008, *ApJ*, 682, 81, doi: [10.1086/588776](https://doi.org/10.1086/588776)
- Shemmer, O., Netzer, H., Maiolino, R., et al. 2004, *ApJ*, 614, 547, doi: [10.1086/423607](https://doi.org/10.1086/423607)
- Shen, Y., Greene, J. E., Strauss, M. A., Richards, G. T., & Schneider, D. P. 2008, *ApJ*, 680, 169, doi: [10.1086/587475](https://doi.org/10.1086/587475)
- Shen, Y., & Ho, L. C. 2014, *Nature*, 513, 210, doi: [10.1038/nature13712](https://doi.org/10.1038/nature13712)
- Shen, Y., & Liu, X. 2012, *ApJ*, 753, 125, doi: [10.1088/0004-637X/753/2/125](https://doi.org/10.1088/0004-637X/753/2/125)
- Shen, Y., Richards, G. T., Strauss, M. A., et al. 2011, *The Astrophysical Journal Supplement Series*, 194, 45, doi: [10.1088/0067-0049/194/2/45](https://doi.org/10.1088/0067-0049/194/2/45)
- Shin, J., Woo, J.-H., Nagao, T., & Kim, S. C. 2013, *ApJ*, 763, 58, doi: [10.1088/0004-637X/763/1/58](https://doi.org/10.1088/0004-637X/763/1/58)
- Timlin, J. D., Brandt, W. N., & Laor, A. 2021, *Monthly Notices of the Royal Astronomical Society*, 504, 5556, doi: [10.1093/mnras/stab1217](https://doi.org/10.1093/mnras/stab1217)
- Timlin, J. D., Brandt, W. N., Ni, Q., et al. 2020, *MNRAS*, 492, 719, doi: [10.1093/mnras/stz3433](https://doi.org/10.1093/mnras/stz3433)
- Trakhtenbrot, B., & Netzer, H. 2012, *MNRAS*, 427, 3081, doi: [10.1111/j.1365-2966.2012.22056.x](https://doi.org/10.1111/j.1365-2966.2012.22056.x)
- Vanden Berk, D. E., Richards, G. T., Bauer, A., et al. 2001, *The Astronomical Journal*, 122, 549, doi: [10.1086/321167](https://doi.org/10.1086/321167)
- Vasudevan, R. V., & Fabian, A. C. 2007, *Monthly Notices of the Royal Astronomical Society*, 381, 1235, doi: [10.1111/j.1365-2966.2007.12328.x](https://doi.org/10.1111/j.1365-2966.2007.12328.x)
- White, R. L., Becker, R. H., Helfand, D. J., & Gregg, M. D. 1997, *The Astrophysical Journal*, 475, 479, doi: [10.1086/303564](https://doi.org/10.1086/303564)
- Wills, B. J., Laor, A., Brotherton, M. S., et al. 1999, *ApJL*, 515, L53, doi: [10.1086/311980](https://doi.org/10.1086/311980)
- Yang, Q., Shen, Y., Liu, X., et al. 2020, *ApJ*, 900, 58, doi: [10.3847/1538-4357/aba59b](https://doi.org/10.3847/1538-4357/aba59b)
- York, D. G., Adelman, J., John E. Anderson, J., et al. 2000, *The Astronomical Journal*, 120, 1579, doi: [10.1086/301513](https://doi.org/10.1086/301513)
- Yuan, Y., Blandford, R. D., & Wilkins, D. R. 2019a, *Monthly Notices of the Royal Astronomical Society*, 484, 4920, doi: [10.1093/mnras/stz332](https://doi.org/10.1093/mnras/stz332)
- Yuan, Y., Spitkovsky, A., Blandford, R. D., & Wilkins, D. R. 2019b, *Monthly Notices of the Royal Astronomical Society*, 487, 4114, doi: [10.1093/mnras/stz1599](https://doi.org/10.1093/mnras/stz1599)
- Zhu, S. F., Brandt, W., & Timlin, J. 2021, in *American Astronomical Society Meeting Abstracts*, Vol. 53, *American Astronomical Society Meeting Abstracts*, 426.06
- Zhu, S. F., Brandt, W. N., Luo, B., et al. 2020, *Monthly Notices of the Royal Astronomical Society*, 496, 245, doi: [10.1093/mnras/staa1411](https://doi.org/10.1093/mnras/staa1411)